Carbon 183 (2021) 940–947

Contents lists available at ScienceDirect

Carbon

journal homepage: www.elsevier.com/locate/carbon

Research Article

Graphitization of low-density amorphous carbon for electrocatalysis electrodes from ReaxFF reactive dynamics

Md Delowar Hossain [a, b], Qing Zhang [b], Tao Cheng [b, c], William A. Goddard III [b, *], Zhengtang Luo [a, **]

[a] Department of Chemical and Biological Engineering, William Mong Institute of Nano Science, and Technology and Hong Kong Branch of Chinese National Engineering Research Center for Tissue Restoration and Reconstruction, The Hong Kong University of Science and Technology, Clear Water Bay, Kowloon, 999077, Hong Kong

[b] Materials and Process Simulation Center (MSC), MC 139-74, California Institute of Technology, Pasadena CA, 91125, USA

[c] Institute of Functional Nano & Soft Materials (FUNSOM), Jiangsu Key Laboratory for Carbon Based Functional Materials & Devices, Soochow University, Suzhou, Jiangsu, 215123, China

ARTICLE INFO

Article history:
Received 16 April 2021
Received in revised form
21 July 2021
Accepted 28 July 2021
Available online 3 August 2021

Keywords:
ReaxFF reactive force field
Reactive dynamics simulations
Graphitization
X-ray diffraction
Raman spectroscopy
Carbon electrode

ABSTRACT

We predict the three-dimensional structure of amorphous carbon generated by heating diamond superlattice at 6000 K with rapid quenching from the liquid phase for densities ranging from 2.0 to 3.5 g/cm^3, in comparison with 2.26 and 3.54 g/cm^3 for bulk graphite and bulk diamond, respectively. These predictions are based on reactive dynamics (RD) simulations using the ReaxFF reactive force field. Here, we simulate the graphitization of amorphous carbon at high temperature to calculate physical properties relevant to conductive carbon supports useful for electrocatalysts. The low-density graphitic materials mostly oriented in the (002) plane with a main X-ray diffraction (XRD) peak between 26 and 28°, as observed experimentally. For low density carbon (2.0–2.5 g/cm^3), we find >90% sp^2 character with ~2-1% sp and <8% sp^3. While for higher density carbon, the amount of sp^2 fraction decreases with density and find 70.0% sp^3 with 29.7% sp^2 and 0.3% sp for 3.4 g/cm^3 density, which can be compared to DLC of 3.24 g/cm^3 density resulting good agreement with XPS experiments. Based on the simulated 3D structure, we create 2D surface slab consisting of various defective sites within the surface. The 2D surface dominates with hexagonal carbon ring along with few pentagon and heptagon rings in the graphitic structure that may be useful as electrocatalysts for different energy conversion reactions.

1. Introduction

Carbon is one of the most abundant and highly used materials. The low cost, lightness, structural diversity, good electrical and thermal conductivity, sufficient stability makes carbon materials unique and popular for very different research fields including electronics, biological sensing, and electrocatalysis [1–6]. Significant advances have been made recently to synthesis carbon-based electrode materials for metal production, energy storage in batteries and supercapacitors, and electrochemical conversion reaction because carbon provides a wide potential window, exhibits chemical inertness, and provides effective supports for catalysts [7–9]. The performance of carbon materials as electrodes mostly arises from its structural polymorphism, surface chemistry, chemical stability, strong internal C–C bond, and ability to bind to surface modifiers. Using a variety of raw materials and synthesis techniques, carbon can produce variety of carbon-based electrode materials including amorphous carbon, diamond like carbon (DLC), graphitic carbon, carbon nanotubes (CNT), vapor deposited carbon films, glassy carbon, and graphene, showing distinct electrochemical properties for various chemical reactions [10–13].

Amorphous and graphitic carbons are ubiquitous as electrode materials because of the strong C–C bonds that depend on synthesis conditions, including three-dimension high density diamond-like-carbon to two-dimensional low density highly conducting graphitic carbon. Tetrahedral amorphous carbon, known as DLC, has a high fraction (~70%) of sp^3 carbon, leading to excellent physical properties, such as high hardness, low friction and wear rate, optical transparency, and chemical inertness [14–18]. DLC

* Corresponding author.
** Corresponding author.
E-mail addresses: wag@caltech.edu (W.A. Goddard), keztluo@ust.hk (Z. Luo).

https://doi.org/10.1016/j.carbon.2021.07.080
0008-6223/

materials have been prepared using a range of deposition methods, including sputtering, ion beams, and plasma enhanced vapor deposition [11]. The inclusion of impurities such as boron or nitrogen can increase the electrical conductivity sufficiently to use as electrode materials for distinct electrochemical applications [19]. On the other hand, an important quite different material is glassy carbon (GC), widely used as an electrode material and synthesized by a variety of techniques. Thus polymeric materials can be carbonized at high temperature, 1000–3000 °C, in an inert atmosphere [20]. The resulting material after carbonization consists of strong C–C sp^2 bonds that form graphitic plane having a 3.6 Å interplanar spacing. This structure consists of randomly intertwined ribbons of graphitic planes [21]. Large surface area mesoporous carbon (MC) is another form of graphitic carbon obtained from carbonization or pyrolysis of carbon rich materials at high temperature. MC is widely used in supercapacitors to provide high storage capacity and in fuel cells to provide a conducting support for metal electrocatalysts [22–24].

The lack of experimental tools to obtain an atomistic characterization to understand the complex carbon structures and their mechanisms of formation motivated the simulations. Tremendous efforts have invested to obtain carbon structure-properties relationship using molecular dynamics (MD) simulation at various scales [25–28]. The ReaxFF reactive force field [29] based on bond-order-dependent interatomic potentials and dynamic charges based charge equilibration (QEq) [30] has proved valuable in describing chemical reaction processes for systems far too large for QM (e.g., high impact decomposition of an energetic materials composite with 3.7 million atoms to find the origin of the hot spot) [31] with modest computational efforts. Li et al. [32] compared the graphitization to form amorphous carbon using Chenoweth [33] and Srinivasan [34] ReaxFF parameter sets, demonstrating the graphitization process with both sets. The latter parameter set showed reasonable agreement with experimental result for mechanical properties [35]. Additionally, they investigated the effect of simulation time steps and temperature on the graphitization of amorphous carbon using ReaxFF MD simulation. They found that a 0.2 fs timestep is sufficient for simulation. The temperature plays a vital role for graphitization, with higher temperature increasing the sp^2 fraction. The carbonization of coke at 1500 °C produces mostly sp^2 with the structure consisting of five membered rings that are responsible for curved graphene layer distortions with additional defects within the structure [36]. Very recently, a similar investigation was carried out by Y. Tian et al. [37] and they found that a coke carbonization process at 3500 K that produces carbon structures with stacking faults leading to wrinkled carbon layers (increased layer spacing containing arc-shaped moieties and numerous dislocations). The effect of ultrafast cooling rate for pure carbon gas at 6000 K and polymer carbonization at 1273 K were investigated by using ReaxFF MD simulations [38,39]. They showed that fast quenching from 6000 to 2500 K produces onion like fullerene molecules. The structure was mostly sp^2 carbon hybridized consisting large amount of hexagon ring along with pentagon and heptagon. The produced amorphous carbon structure significantly depends on the parent carbon source such as high temperature carbonization of polyacrylonitrile (PAN) results gases species like N_2, H_2, NH_3, HCN along with 5–7 members ring carbon structure [40]. Beyond carbonization, ReaxFF simulation of Laser-Induced Graphene (LIG) obtained from irradiation of polymer films result amorphous structure containing significant number of 5–7 members carbon ring with largest surface area [41].

Here we are interested in the high temperature carbon graphitization process that leads to highly conducting graphite-like surfaces that is very useful as support materials for heterogenous catalysts and electrocatalysts. Graphitization is a widely known process with many experiments, but the information regarding atomistic structure formation mechanism during heat treatment are quite unclear. To provide fundamental understanding about the atomistic structure and properties relationship, we conduct graphitization process of amorphous carbon computationally by quenching very rapidly from a molten state to room temperature. Based on this detailed atomistic structural information about bonding and coordination, we calculate various properties in particular the relationship between the graphitization process, the density, and the measurable properties such as X-ray diffraction pattern, Raman shifts, radial distribution functions, hybridization for comparison with experiments. Such comparisons may allow us to understand the nature of the carbon electrode materials synthesized experimentally, by chemical vapor deposition (CVD) or thermal annealing. Experimental characterization of carbon electrode materials with different densities is not well established, so we want to examine how carbon with various densities is related to synthetic graphitic carbon and how this determines their various properties. Experimentalist should choose lower density carbon for higher conductivity requirement such as electrocatalysis as it consists of more sp^2 carbon. The well known sources of amorphous carbon are coke, coal, graphene oxides, graphite etc. Earlier, we reported the results on forming Hydrogen-free diamond-like carbon (DLC), where the predicted density (3.24 g/cm^3) and fraction of sp^3 carbon (70%) are both in good agreement with experiment [17]. In this work, we found that low-density carbon has a tendency to produce disoriented graphene layers, giving rise to the (002) plane in the X-ray diffraction (XRD) peak between 26 and 28°. Our Raman intensity calculations demonstrates the presence of characteristic D, G, and 2D peaks for graphitic samples whose ratios depend on density. Moreover, we find that the atoms in low density carbon (2.0–2.5 g/cm^3) are mostly sp^2 character (>90%) in contrast to dense carbon (DLC at 3.24 g/cm^3) which is 70.3% sp^3 character.

2. Methodology

In order to make unbiased predictions of the atomistic structure of both bulk amorphous carbon and its surface, we used the ReaxFF [17,18,42] in reactive dynamics (RD) simulations (Tables S1–S2, Fig. S1). Previous studies have also used this ReaxFF to describe reactions using amorphous carbon systems and found the comparable results with experiments [17,18,43]. We started graphitization process with the 3D structure of amorphous carbon obtained from previous work [17,18] containing 4096 atoms in the 8 × 8 × 8 superlattice of diamond MD simulation system. We heated the system at a heating rate of 600 K/ps from 10 K and continued for 5 ps at 6000 K and then quenched to 300 K at rate of 1400 K/ps, followed by equilibration at 300 K for 100 ps to obtain amorphous carbon. This amorphous carbon system was then reheated to 3500 K at 350 K/ps to simulate graphitization conditions and equilibrated for 100 ps at 3500 K. Finally, the system was quenched again to 300 K, but now more slowly, at a rate of 100 K/ps, and equilibrated for 200 ps. We also carried out simulation with relatively lower supercell of 4 × 4 × 4 containing 512 carbon atoms without reheated at 3500 K (graphitization condition) temperature (results are shown in supplementary information). All simulations were conducted using LAMMPS package [44] using a 0.2 fs simulation time step with 3D periodic boundary conditions. The default Nose–Hoover thermostat in LAMMPS was used to control temperature with a thermostat time constant set at 100 fs. All the simulations were carried out using the NVT ensemble to control density, followed by the NPT ensemble to compare pressure [32,45]. The X-ray powder diffraction patterns were simulated with BIOVIA materials studio (v7) reflex [46] modelling software. XRD patterns were collected using an X-ray powder diffractometer with

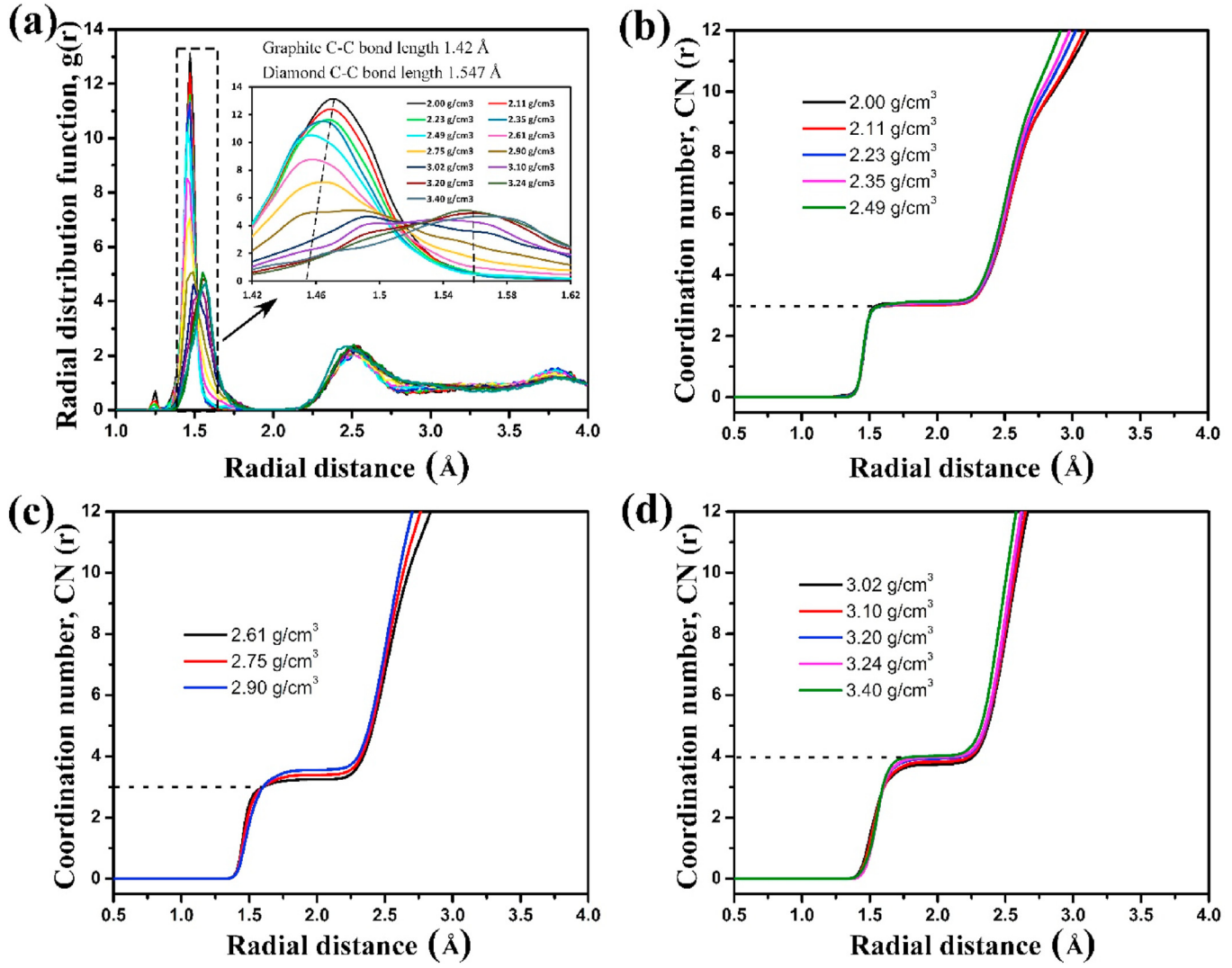

Fig. 1. Radial distribution function of carbon structure for various densities. (a) the carbons with density 2.90 g/cm^3 and below shows a C–C bond at 1.46 Å indicating graphitic sp^2 character while carbon with densities of 3.0 g/cm^3 and larger show a C–C peak at 1.56 Å, indicating diamond sp^3 character. (b–d) the coordination number varies with carbon density. (A colour version of this figure can be viewed online.)

Cu-Kα radiation source of 1.5406 Å wavelength. X-ray diffraction peaks were measured in the angular range of $10° \leq 2\theta \leq 90°$ in a step-scan mode (0.05°/step). The Raman shift for different carbon density samples after graphitization of amorphous carbon were carried out using the two Phase Thermodynamic (2 PT) method [47–49], which uses the Fourier transform of the velocity auto-correlation function to obtain the vibrational power spectrum. We used NVT dynamics for 20 ps at 2 fs timestep to generate LAMMPS trajectory. The trajectory then used to produce a file contains the 3n degrees of freedom as a function of frequency after applying 2 PT analysis. We used commercially available VESTA software for visualizing the system [50].

3. Results and discussion

Density is a most important factor in determining the carbon structures used as electrode for energy storage and electrocatalysis applications [51–54]. The diamond crystal has a density of 3.54 g/cm^3, which can be compared to 3.24 for DLC, while density of bulk graphite is 2.26 g/cm^3. The density of graphitized carbon depends on such factors as volatile matter containing within the carbon sources, heating rate, and carbonization temperature. We studied a simulation box with 4096 carbon atoms with density varying from 2.0 to 3.40 g/cm^3 to cover the ranges of experimental carbon electrode system. We use the potential energy from the RD simulations as an indicator of structural relaxation and stability. The potential energy per carbon of graphitic carbon as a function of density indicates that a carbon density of 2.49 g/cm^3 shows most stable density configuration among the systems studied (**Fig. S2**). The potential energy per carbon varies between −8.25 and −8.39 eV for various carbon densities, which is little lower than the value of −8.53 eV for graphene and −8.73 eV for diamond ReaxFF simulation. The simulations are equilibrated for 200 ps at 300 K and found almost linear potential energy change (Fig. S3). Moreover, the potential energy per atom shows comparable with other ReaxFF (Fig. S4). The energy profile of the initial amorphous carbon (without graphitization) as a function of density at various cooling rates is shown in Fig. S5. The rate of cooling effects on stabilization of carbon shows that slower cooling rate leads to more stable amorphous structures than the faster rate. Fig. 1 shows the radial distribution function (RDF) and coordination number (CN) as a function of carbon densities. Fig. 1a shows that carbon structure

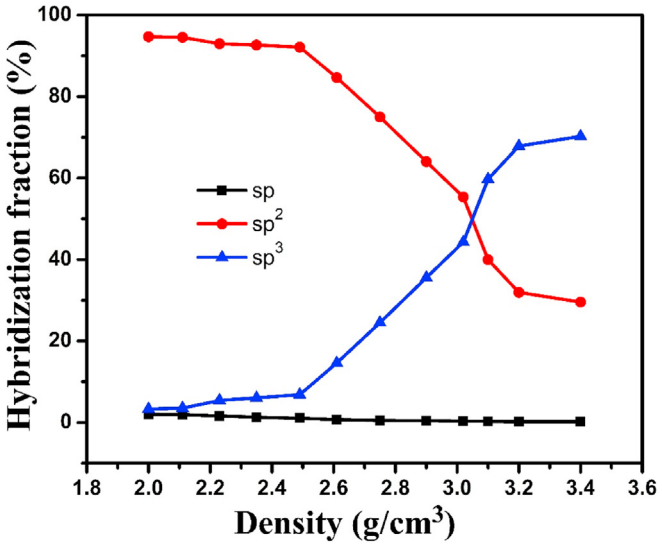

Fig. 2. The hybridization fractions as a function of density for carbon system after graphitization and annealing at 3500 K and 300 K respectively. The sp^2 characters dominates for low density carbons until it reaches to 3.05 g/cm^3 where it shows less graphitic character. By 3.4 g/cm^3 the amount of sp^3 character is increased to 70%, compared to 100% for diamond at 3.54 g/cm^3. (A colour version of this figure can be viewed online.)

with density <2.90 g/cm^3 lead to a main peak at a C–C bond of ~1.46 Å, compared to 1.42 Å for graphitic C-C bond (inset figure), with an average of 3 bonds per C, as expected for sp^2. On the other hand, for carbon density >2.90 g/cm^3 the C–C distance is ~1.56 Å and the average number of bonds is 4 as expected of sp^3 for DLC or diamond. A tiny peak at ~1.22 Å for low carbon density indicates the presence of triple bonds with sp character. Another peak at around 2.5 Å moves to a shorter interatomic distance with increasing carbon density, indicating that atoms are stacked more closer to each other. Fig. 1b–d shows the coordination number for different density carbon structure. Fig. 1b indicates that at 1.46 Å a sharp rise of coordination number and give a plateau at around 3 CN for carbon structure containing density of 2.0–2.49 g/cm^3, indicating sp^2 graphitic carbon. The plateau for coordination number at 1.52 Å is increasing with carbon density and found CN lies between 3 and 4 due to rise of sp^3 character for carbon density between 2.61–2.90 g/cm^3 (Fig. 1c). Finally, a sharp rise of CN observes at 1.56 Å and gives a plateau around 4, characteristic of diamond like carbon, for carbon density of 3.02–3.40 g/cm^3, indicating that sp^3 character becomes majority in their corresponding structures (Fig. 1d). The RDF profiles for the initial amorphous carbon (without graphitization) with 2.49 g/cm^3 and 3.24 g/cm^3 density is shown in Fig. S6.

The hybridization fractions of carbon atoms having sp^3, sp^2, or sp character were evaluated using a cutoff bond distance of 1.85 Å based on Fig. 1. Fig. 2 shows the variation in the sp, sp^2 and sp^3 fraction for carbon structures after the graphitization process. We

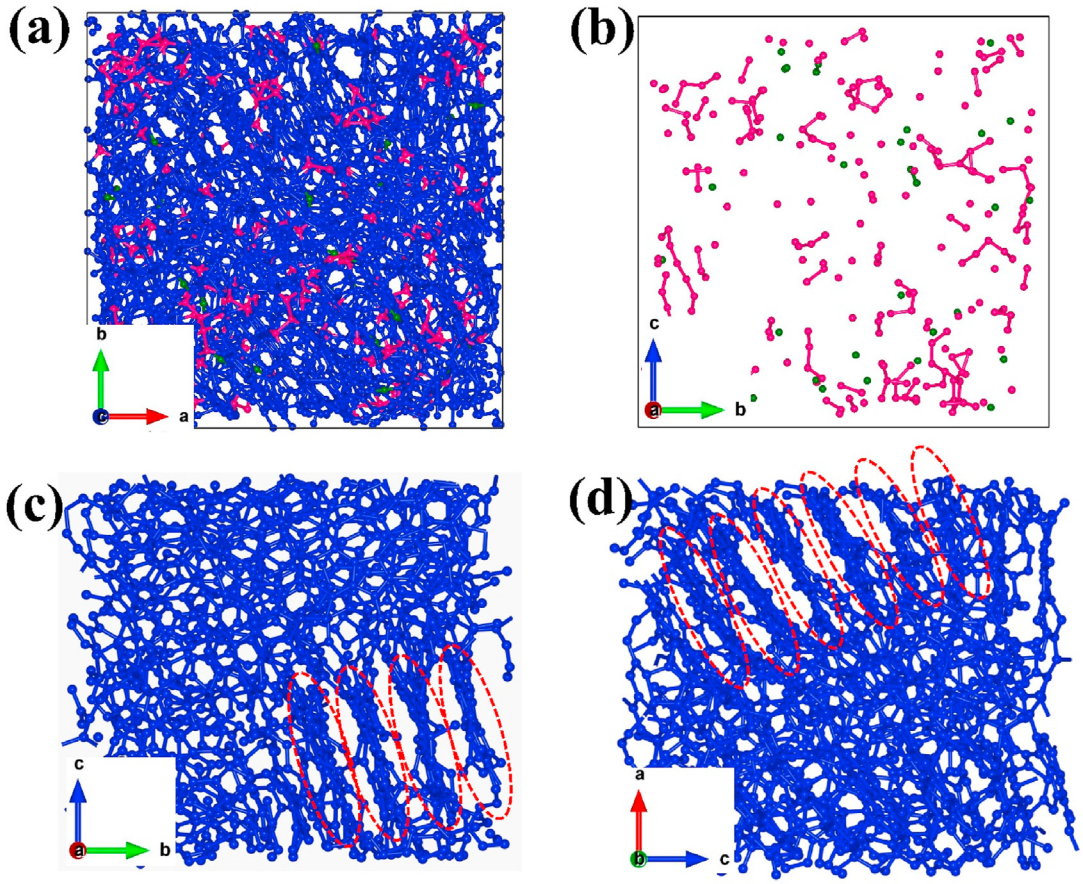

Fig. 3. Structure of bulk carbon after graphitization process for a density of 2.49 g/cm^3 sp^2 C atoms: blue (92.13%); sp^3 C atoms: pink (6.83%); sp C atoms: green (1.04%). (a) total, (b) sp^3+sp, (c, d) sp^2 at different orientation. (A colour version of this figure can be viewed online.)

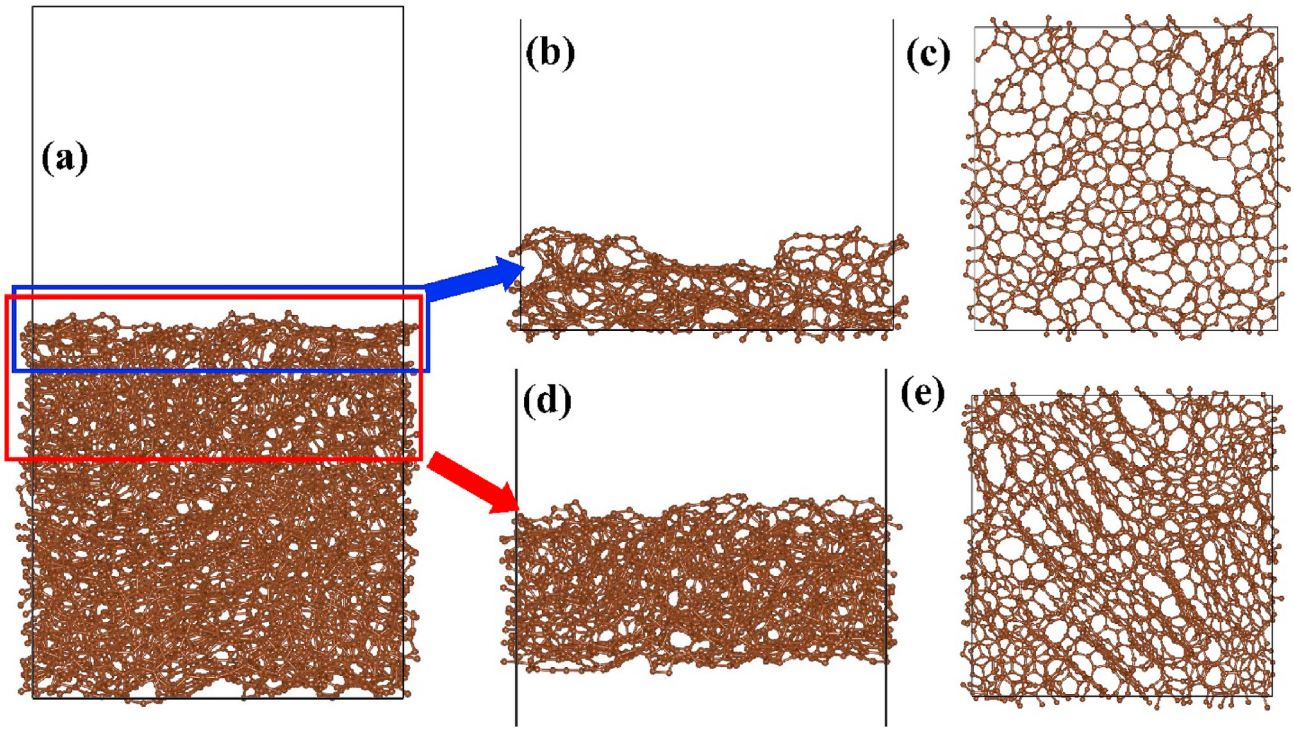

Fig. 4. 2D surface structure of graphitic carbon after graphitization process for a density of 2.49 g/cm^3 (a) structure containing 4096 carbon atoms shows mostly sp^2 C atoms, (b, c) small thin layer (708 carbon atoms) of surface mainly consists of various carbon defects and different carbon membered rings, and (d, e) relatively bigger surface structure containing 1724 carbon atoms showing various defects and dislocations on the surface causing irregular orientation carbon layers. (A colour version of this figure can be viewed online.)

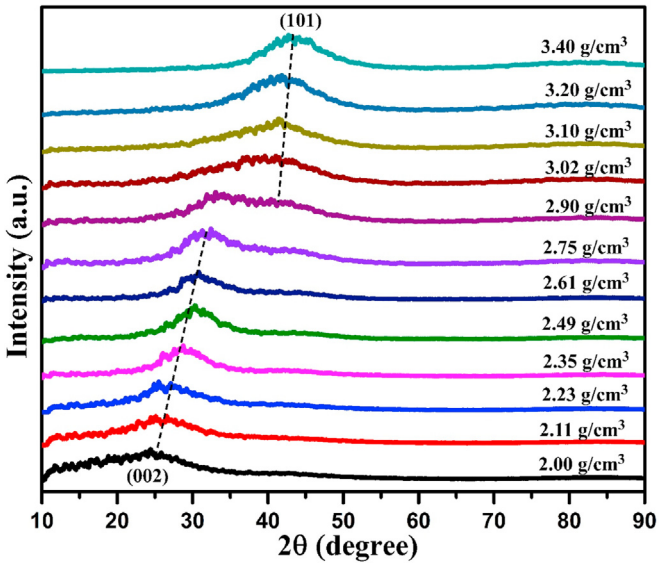

Fig. 5. Predicted X-ray diffraction pattern for simulated carbon structure at various densities. For densities of 2.11–2.23 g/cm^3 the graphitic peak for (002) is observed at 26°, which shifts linearly to 32° for 2.75 g/cm^3 as the sp^2 C fraction decreases. Then for 2.9 g/cm^3 we observe a very broad peak from 33° to 40°. But for 3.0–3.4 g/cm^3 this 2nd peak shifts gradually from 40° to 45° corresponding to diamond like carbon with more sp^3 C fraction. (A colour version of this figure can be viewed online.)

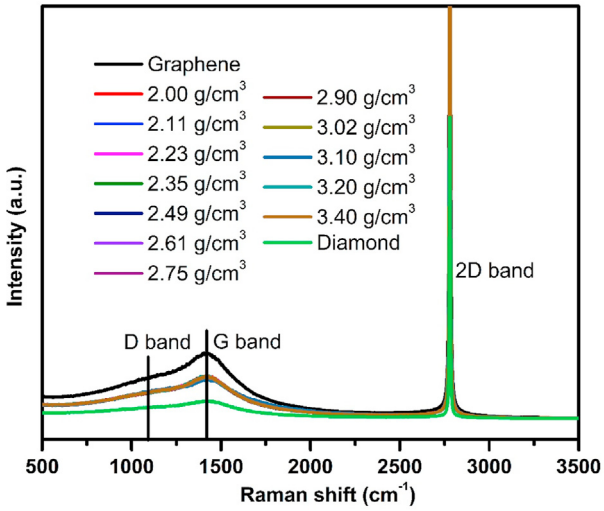

Fig. 6. Raman spectra for graphitized carbon at various densities. The peaks at 1140 cm^{-1}, 1450 cm^{-1} and 2778 cm^{-1} correspond to the carbon characteristics D, G and 2D band. (A colour version of this figure can be viewed online.)

see that the sp^2 character is >90% up 2.0–2.49 g/cm^3 carbon density and decreases linearly with increasing density and reach to 29.7% for 3.4 g/cm^3. Oppositely, the sp^3 character increases from 4% for 2.0 g/cm^3 to 70% for 3.4 g/cm^3. The sp character varies from 2.0% to 0.3% when density increases from 2.0 to 3.4 g/cm^3. Li et al. [25] studied the graphitization process at 3500 K for amorphous carbon containing 2000 atoms using ReaxFF and observed 92% sp^2 character for 2.20 g/cm^3 carbon density after simulation for 200 ps. Similar observations were made by de Tomas et al. [45]. They used environment-dependent interaction potential (EDIP) for amorphous carbon simulations, quenching from the liquid with subsequent annealing. After 200 ps simulation, they found 2.5% sp, 93.9% sp^2 and 4.6% sp^3 for 2.0 g/cm^3 carbon density while the amount of

sp^2 fraction decreases with increasing density. They predicted 0.2% sp, 39.6% sp^2 and 60.2% sp^3 for carbon with density 3.0 g/cm^3. Our obtained result showed comparable with above mentioned literatures. The experimental results show that sp^3 varies from 8% for 2.0 g/cm^3 to 87% for 3.1 g/cm^3 carbon density [55,56]. This little discrepancy with our results could be due to use of diamond like carbon for experiment (no heat treatment done). However, our simulation results show reasonable agreement with experiment for high density carbon (3.4 g/cm^3) system without graphitization process containing more than 85% sp^3 fraction when annealed slowly (Fig. S7).

Fig. 3 shows the topography of bulk carbon structures at density of 2.49 g/cm^3 containing 4096 atoms. The bulk structure contains 92.13% sp^2 C, 6.83% sp^3 C and 1.04% sp C after graphitization at 3500 K. Fig. 3a shows the distribution of sp^2 (blue), sp^3 (pink) and sp (green) character within the 2.49 g/cm^3 carbon bulk structure after graphitization. We find that most of the sp^2 C atoms interconnect to form graphite layers with dislocation defects. The distorted graphite layers interconnect with short, branched chains (Fig. 3b) of sp^3 atoms. Occasional sp atoms are found bonded with sp^2 atoms (allene-like) and sometimes bonded to each other (acetylene-like). Fig. 3c and d shows the sp^2 C atoms which mostly interconnect to form hexagons as in graphite. However, the layer spacing does not match with normal graphite layer distance (3.34 Å). Moreover, chemical bonding and Π-Π stacking are observed between dislocated carbon layers and aliphatic/linear carbon atoms. Several studies reported earlier that this irregular carbon layers may arise due to crystal defects containing five to eight members carbon rings, limited space, screw dislocation within the structure. The presence of crystal defects such as five-eight carbons ring causes irregular stacking of graphite layers called “wrinkled carbon layers” [36,37,57]. At the same time, the limited space causes folding and distortion in the graphite layers. The screw dislocations within the structure are also responsible for the distortion of graphite layers. We observe several parallel graphene-like layers in various regions with different orientations (red dot circles) [32]. Structure of amorphous carbon (without heated at graphitization temperature) for different carbon densities are shown in Figs. S8–S16. We find relatively improved atomic packing within the crystalline regions after graphitization compared to the amorphous structure.

The bulk structure for 2.49 g/cm^3 carbon were cut into two-dimensional (2D) surface at different thickness are shown in Fig. 4. We consider 30 Å vacuum in z direction and apply same graphitization process during simulation as for bulk structure. Fig. 4a shows the 2D surface structure containing 4096 atoms consisting mostly sp^2 character and graphitic in nature. The top surface was separately simulated (708 atoms) and found lots of defects, and mixture of various carbon ring ranging from 4-8-carbon (Fig. 4b and c). Similar findings also observe for simulation results containing 1724 atoms shown in Fig. 4d and e. The surface consists various structural defects and dislocations often results irregular graphite layers. The lack of carbon atoms (4–5 members ring) in the six members ring causes an arched moiety within the structure and responsible for the distortion of regular graphite layers. Similarly, more than six carbons in the ring (7–8) creates a non-planner saddle-shaped moiety, resulting irregular graphite layers in the surface. The presence of 4–8 members carbon ring are also reported for high temperature carbonization using reactive MD simulations [25,36,37,58] and experimental literatures [59–61].

Fig. 5 shows the X-ray diffraction (XRD) pattern for various carbon densities obtained after graphitization. There are two main peaks characteristic of graphitic carbon (002) observed at 26° diffraction angle and (101) at 44.5° (Fig. S17), which are in good agreement with previous simulation results [36] and experimental observation [62,63]. At low density, the (002) diffraction peak at 26° is dominant, corresponding with the major peak obtained for experimentally synthesized graphite. The sp^2 C fractions dominate until 3.02 g/cm^3 carbon density, indicating graphite in nature (Fig. 2), which is confirmed by the presence of graphitic characteristic dominant peak for (002) plane. The graphitic carbon (002) peak gradually disappears due to decreases of the sp^2 C fraction while the peak at 44.5° becomes dominant for sp^3 C hybridization above 3.02 g/cm^3 density, indicating the presence of the diamond like carbon as the density is increased.

We predicted the Raman shift after the graphitization process for amorphous carbon using the two Phase Thermodynamic (2 PT) method. 2 PT uses the Fourier transform of the velocity autocorrelation function to obtain the vibrational density of states. Fig. 6 shows the shift of the Raman spectroscopy lines for various carbon densities comparing to graphite and diamond. We find the characteristic peaks for carbon structures, but the peaks change little with carbon densities. The peak at 1140 cm^{-1}, 1450 cm^{-1}, and 2778 cm^{-1} corresponds to D, G and 2D band carbon materials. The Raman spectrum calculations deviated little from experiment, probably because ReaxFF focusses on bond breaking not force constants. The D-peak also known as disorder peak mainly originated from structural defects within the graphite structure. It also indicates the sign of symmetry breakdown in the graphite lattice. While the graphite peak, denoted by G is originated from the doubly degenerate zone-center phonon E_{2g} mode and corresponds to C–C stretching mode [11,64,65]. The G peak intensity represents the order of graphitization and the decrease of peak intensity with increasing the carbon density indicates transition of graphite carbon to diamond like carbon as discussed earlier.

4. Summary

Using ReaxFF RMD simulations, we constructed hydrogen-free amorphous carbon structures for densities in the range of 2.0–3.4 g/cm^3. We predict sp^2 hybridization for density <3.0 g/cm^3 and sp^3 for higher density after graphitization in good agreement with experiment. This indicates that quenching from the melt using ReaxFF, followed by graphitization leads to amorphous carbon systems with properties close to those synthesized experimentally.

We found that low density carbon (2.0–2.5 g/cm^3) has >90% sp^2 characters with ~2-1% sp and <8% sp^3. As the density is gradually increased to 3.4 g/cm^3 we find 70.3% sp^3 with 29.5% sp^2 and 0.2% sp, showing good agreement with XPS experiments [66,67]. This agreement with experiment was confirmed further with X-ray diffraction and radial distribution functions (RDF). Thus, low-density graphitic materials are dominated by the (002) plane with a main X-ray diffraction (XRD) peak between 26 and 30° as observed experimentally. The G peak intensity decreases with increasing the carbon density indicates transition of graphite carbon to diamond like carbon, is consistent with others calculated characterization.

CRediT authorship contribution statement

Md Delowar Hossain: Conceptualization, Methodology, Investigation, Data analysis, Visualization, Writing – original draft. **Qing Zhang:** Data analysis, Review & Editing, Discussion. **Tao Cheng:** Data analysis, Review & Editing, Discussion. **William A. Goddard:** Supervision, Project administration, and Revision. **Zhengtang Luo:** Supervision, Project administration, and Revision. All authors approved the final version of the manuscript.

Declaration of competing interest

The authors declare that they have no known competing financial interests or personal relationships that could have appeared to influence the work reported in this paper.

Acknowledgement

M.D.H and Z.L. acknowledge funds from Research Grant Council of Hong Kong SAR (16304518), NSFC-RGC Joint Research Scheme (N_HKUST607/17), Zhongshan City Bureau of Science and Technology (2019AG018), the IER foundation (HT-JD-CXY-201907). "International science and technology cooperation projects" of Science and Technological Bureau of Guangzhou Huangpu District (2019GH06), Guangdong Science and Technology Department (Project#:2020A0505090003), Research Fund of Guangdong-Hong Kong-Macao Joint Laboratory for Intelligent Micro-Nano Optoelectronic Technology (No. 2020B1212030010).

The Caltech efforts were supported by NSF (CBET-1805022) and ONR (N00014-18-1-2155).

Appendix A. Supplementary data

Supplementary data to this article can be found online at https://doi.org/10.1016/j.carbon.2021.07.080.

References

[1] S. Han, D. Wu, S. Li, F. Zhang, X. Feng, Porous graphene materials for advanced electrochemical energy storage and conversion devices, Adv. Mater. 26 (2014) 849–864.
[2] J. Tang, J. Liu, N.L. Torad, T. Kimura, Y. Yamauchi, Tailored design of functional nanoporous carbon materials toward fuel cell applications, Nano Today 9 (2014) 305–323.
[3] Z. Yang, J. Ren, Z. Zhang, X. Chen, G. Guan, L. Qiu, Y. Zhang, H. Peng, Recent advancement of nanostructured carbon for energy applications, Chem. Rev. 115 (2015) 5159–5223.
[4] W. Zhang, S. Zhu, R. Luque, S. Han, L. Hu, G. Xu, Recent development of carbon electrode materials and their bioanalytical and environmental applications, Chem. Soc. Rev. 45 (2016) 715–752.
[5] A. Nsabimana, J. Lai, S. Li, P. Hui, Z. Liu, G. Xu, Surfactant-free synthesis of three-dimensional nitrogen-doped hierarchically porous carbon and its application as an electrode modification material for simultaneous sensing of ascorbic acid, dopamine and uric acid, Analyst 142 (2017) 478–484.
[6] M.D. Angione, R. Pilolli, S. Cotrone, M. Magliulo, A. Mallardi, G. Palazzo, L. Sabbatini, D. Fine, A. Dodabalapur, N. Cioffi, Carbon based materials for electronic bio-sensing, Mater. Today 14 (2011) 424–433.
[7] Y. Xu, M. Kraft, R. Xu, Metal-free carbonaceous electrocatalysts and photocatalysts for water splitting, Chem. Soc. Rev. 45 (2016) 3039–3052.
[8] Q. Wu, L. Yang, X. Wang, Z. Hu, From carbon-based nanotubes to nanocages for advanced energy conversion and storage, Acc. Chem. Res. 50 (2017) 435–444.
[9] M. Zhou, H.-L. Wang, S. Guo, Towards high-efficiency nanoelectrocatalysts for oxygen reduction through engineering advanced carbon nanomaterials, Chem. Soc. Rev. 45 (2016) 1273–1307.
[10] J. Lai, A. Nsabimana, R. Luque, G. Xu, 3D porous carbonaceous electrodes for electrocatalytic applications, Joule 2 (2018) 76–93.
[11] R.L. McCreery, Advanced carbon electrode materials for molecular electrochemistry, Chem. Rev. 108 (2008) 2646–2687.
[12] Ljubisa, in: Chemistry and physics of carbon, in: R. Radovic (Ed.) 27, Marcel Dekker, Inc., New York, 2001, p. 416. +XV. ISBN 0-8247-0246-8. $225, Energy & Fuels, 15 (2001) 502-502.
[13] R.L. McCreery, Electroanalytical Chemistry, vol. 17, Marcel Dekker, Inc., New York, 1991, pp. 221–374.
[14] D.-W. Kim, K.-W. Kim, Effects of sliding velocity and normal load on friction and wear characteristics of multi-layered diamond-like carbon (DLC) coating prepared by reactive sputtering, Wear 297 (2013) 722–730.
[15] Y. Liu, B. Yu, Z. Cao, P. Shi, N. Zhou, B. Zhang, J. Zhang, L. Qian, Probing superlubricity stability of hydrogenated diamond-like carbon film by varying sliding velocity, Appl. Surf. Sci. 439 (2018) 976–982.
[16] D. Wu, S. Ren, J. Pu, Z. Lu, G. Zhang, L. Wang, A comparative study of tribological characteristics of hydrogenated DLC film sliding against ceramic mating materials for helium applications, Appl. Surf. Sci. 441 (2018) 884–894.
[17] C. Matta, L. Joly-Pottuz, M.I. De Barros Bouchet, J.M. Martin, M. Kano, Q. Zhang, W.A. Goddard, Superlubricity and tribochemistry of polyhydric alcohols, Phys. Rev. B 78 (2008), 085436.
[18] J.-M. Martin, M.-I.D.B. Bouchet, C. Matta, Q. Zhang, W.A. Goddard, S. Okuda, T. Sagawa, Gas-phase lubrication of ta-C by glycerol and hydrogen peroxide. Experimental and computer modeling, J. Phys. Chem. C 114 (2010) 5003–5011.
[19] G. Swain, Electroanalytical Chemistry, AJ Bard and I, Rubinstein, 2003.
[20] G.M. Jenkins, A. Jenkins, K. Kawamura, Polymeric Carbons: Carbon Fibre, Glass and Char, Cambridge University Press, 1976.
[21] M.T. McDermott, C.A. McDermott, R.L. McCreery, Scanning tunneling microscopy of carbon surfaces: relationships between electrode kinetics, capacitance, and morphology for glassy carbon electrodes, Anal. Chem. 65 (1993) 937–944.
[22] M. Zhou, J. Ding, L.-p. Guo, Q.-k. Shang, Electrochemical behavior of L-cysteine and its detection at ordered mesoporous carbon-modified glassy carbon electrode, Anal. Chem. 79 (2007) 5328–5335.
[23] H.-Q. Li, J.-Y. Luo, X.-F. Zhou, C.-Z. Yu, Y.-Y. Xia, An ordered mesoporous carbon with short pore length and its electrochemical performances in supercapacitor applications, J. Electrochem. Soc. 154 (2007) A731.
[24] V. Raghuveer, A. Manthiram, Mesoporous carbons with controlled porosity as an electrocatalytic support for methanol oxidation, J. Electrochem. Soc. 152 (2005) A1504.
[25] X. Li, H. Mizuseki, S.J. Pai, K.-R. Lee, Reactive molecular dynamics simulation of the amorphous carbon growth: effect of the carbon triple bonds, Comput. Mater. Sci. 169 (2019) 109143.
[26] X. Li, P. Ke, K.-R. Lee, A. Wang, Molecular dynamics simulation for the influence of incident angles of energetic carbon atoms on the structure and properties of diamond-like carbon films, Thin Solid Films 552 (2014) 136–140.
[27] T.-B. Ma, Y.-Z. Hu, H. Wang, Molecular dynamics simulation of shear-induced graphitization of amorphous carbon films, Carbon 47 (2009) 1953–1957.
[28] Y.-N. Chen, T.-B. Ma, Z. Chen, Y.-Z. Hu, H. Wang, Combined effects of structural transformation and hydrogen passivation on the frictional behaviors of hydrogenated amorphous carbon films, J. Phys. Chem. C 119 (2015) 16148–16155.
[29] A.C. Van Duin, S. Dasgupta, F. Lorant, W.A. Goddard, ReaxFF: a reactive force field for hydrocarbons, J. Phys. Chem. 105 (2001) 9396–9409.
[30] A.K. Rappe, W.A. Goddard, Charge equilibration for molecular dynamics simulations, J. Phys. Chem. 95 (1991) 3358–3363.
[31] Q. An, S.V. Zybin, W.A. Goddard, A. Jaramillo-Botero, M. Blanco, S.-N. Luo, Elucidation of the dynamics for hot-spot initiation at nonuniform interfaces of highly shocked materials, Phys. Rev. B 84 (2011) 220101.
[32] K. Li, H. Zhang, G. Li, J. Zhang, M. Bouhadja, Z. Liu, A.A. Skelton, M. Barati, ReaxFF molecular dynamics simulation for the graphitization of amorphous carbon: a parametric study, J. Chem. Theor. Comput. 14 (2018) 2322–2331.
[33] K. Chenoweth, A.C. Van Duin, W.A. Goddard, ReaxFF reactive force field for molecular dynamics simulations of hydrocarbon oxidation, J. Phys. Chem. 112 (2008) 1040–1053.
[34] S.G. Srinivasan, A.C. Van Duin, P. Ganesh, Development of a ReaxFF potential for carbon condensed phases and its application to the thermal fragmentation of a large fullerene, J. Phys. Chem. 119 (2015) 571–580.
[35] B.D. Jensen, K.E. Wise, G.M. Odegard, Simulation of the elastic and ultimate tensile properties of diamond, graphene, carbon nanotubes, and amorphous carbon using a revised ReaxFF parametrization, J. Phys. Chem. 119 (2015) 9710–9721.
[36] K. Li, H. Li, M. Sun, J. Zhang, H. Zhang, S. Ren, M. Barati, Atomic-scale understanding about coke carbon structural evolution by experimental characterization and ReaxFF molecular dynamics, Energy Fuel. 33 (2019) 10941–10952.
[37] Y. Tian, G.-Y. Li, H. Zhang, J.-P. Wang, Z.-Z. Ding, R. Guo, H. Cheng, Y.-H. Liang, Molecular basis for coke strength: stacking-fault structure of wrinkled carbon layers, Carbon 162 (2020) 56–65.
[38] N. Orekhov, G. Ostroumova, V. Stegailov, High temperature pure carbon nanoparticle formation: validation of AIREBO and ReaxFF reactive molecular dynamics, Carbon 170 (2020) 606–620.
[39] T. Kato, Y. Yamada, Y. Nishikawa, H. Ishikawa, S. Sato, Carbonization Mechanisms of Polyimide: Methodology to Analyze Carbon Materials with Nitrogen, Oxygen, Pentagons, and Heptagons, Carbon, 2021.
[40] B. Saha, G.C. Schatz, Carbonization in polyacrylonitrile (PAN) based carbon fibers studied by ReaxFF molecular dynamics simulations, J. Phys. Chem. B 116 (2012) 4684–4692.
[41] A. Vashisth, M. Kowalik, J.C. Gerringer, C. Ashraf, A.C.T. van Duin, M.J. Green, ReaxFF simulations of laser-induced graphene (LIG) formation for multifunctional polymer nanocomposites, ACS Applied Nano Materials 3 (2020) 1881–1890.
[42] A.C.T. van Duin, S. Dasgupta, F. Lorant, W.A. Goddard, ReaxFF: A reactive force field for hydrocarbons, J. Phys. Chem. 105 (2001) 9396–9409.
[43] Z. Zhao, M.D. Hossain, C. Xu, Z. Lu, Y.-S. Liu, S.-H. Hsieh, I. Lee, W. Gao, J. Yang, B.V. Merinov, W. Xue, Z. Liu, J. Zhou, Z. Luo, X. Pan, F. Zaera, J. Guo, X. Duan, W.A. Goddard, Y. Huang, Tailoring a three-phase microenvironment for high-performance oxygen reduction reaction in proton exchange membrane fuel cells, Matter 3 (2020) 1774–1790.
[44] S. Plimpton, Fast parallel algorithms for short-range molecular dynamics, J. Comput. Phys. 117 (1995) 1.
[45] C. de Tomas, I. Suarez-Martinez, N.A. Marks, Graphitization of amorphous carbons: a comparative study of interatomic potentials, Carbon 109 (2016) 681–693.

[46] M.A. Neumann, X-Cell, A novel indexing algorithm for routine tasks and difficult cases, J. Appl. Crystallogr. 36 (2003) 356–365.
[47] S.-T. Lin, M. Blanco, W.A. Goddard III, The two-phase model for calculating thermodynamic properties of liquids from molecular dynamics: validation for the phase diagram of Lennard-Jones fluids, J. Chem. Phys. 119 (2003) 11792–11805.
[48] S.-T. Lin, P.K. Maiti, W.A. Goddard III, Two-phase thermodynamic model for efficient and accurate absolute entropy of water from molecular dynamics simulations, J. Phys. Chem. B 114 (2010) 8191–8198.
[49] T.A. Pascal, S.-T. Lin, W.A. Goddard III, Thermodynamics of liquids: standard molar entropies and heat capacities of common solvents from 2PT molecular dynamics, Phys. Chem. Chem. Phys. 13 (2011) 169–181.
[50] K. Momma, F. Izumi, VESTA 3 for three-dimensional visualization of crystal, volumetric and morphology data, J. Appl. Crystallogr. 44 (2011) 1272–1276.
[51] S. Wu, Y. Zhu, Highly densified carbon electrode materials towards practical supercapacitor devices, Science China Materials 60 (2017) 25–38.
[52] E. Taer, A. Apriwandi, Minarni Krisman, R. Taslim, A. Agustino, A. Afrianda, The physical and electrochemical properties of activated carbon electrode made from pandanus tectorius, J. Phys. Conf. 1120 (2018), 012006.
[53] J. Yang, Y. Liu, X. Chen, Z. Hu, G. Zhao, Carbon electrode material with high densities of energy and power, Acta Phys. Chim. Sin. 24 (2008) 13–19.
[54] R.C. Alkire, P.N. Bartlett, J. Lipkowski, Electrochemistry of Carbon Electrodes, John Wiley & Sons2015.
[55] J. Schwan, S. Ulrich, H. Roth, H. Ehrhardt, S. Silva, J. Robertson, R. Samlenski, R. Brenn, Tetrahedral amorphous carbon films prepared by magnetron sputtering and dc ion plating, J. Appl. Phys. 79 (1996) 1416–1422.
[56] J. Robertson, Diamond-like carbon, Pure Appl. Chem. 66 (1994) 1789–1796.
[57] G. Ostroumova, N. Orekhov, V. Stegailov, Reactive molecular-dynamics study of onion-like carbon nanoparticle formation, Diam. Relat. Mater. 94 (2019) 14–20.
[58] T. Kato, Y. Yamada, Y. Nishikawa, H. Ishikawa, S. Sato, Carbonization mechanisms of polyimide: Methodology to analyze carbon materials with nitrogen, oxygen, pentagons, and heptagons, Carbon 178 (2021) 58–80.
[59] C.-T. Toh, H. Zhang, J. Lin, A.S. Mayorov, Y.-P. Wang, C.M. Orofeo, D.B. Ferry, H. Andersen, N. Kakenov, Z. Guo, I.H. Abidi, H. Sims, K. Suenaga, S.T. Pantelides, B. Özyilmaz, Synthesis and properties of free-standing monolayer amorphous carbon, Nature 577 (2020) 199–203.
[60] Ç.Ö. Girit, J.C. Meyer, R. Erni, M.D. Rossell, C. Kisielowski, L. Yang, C.-H. Park, M.F. Crommie, M.L. Cohen, S.G. Louie, A. Zettl, Graphene at the edge: stability and dynamics, Science 323 (2009) 1705–1708.
[61] J. Lahiri, Y. Lin, P. Bozkurt, I.I. Oleynik, M. Batzill, An extended defect in graphene as a metallic wire, Nat. Nanotechnol. 5 (2010) 326–329.
[62] T. Qiu, J.-G. Yang, X.-J. Bai, Y.-L. Wang, The preparation of synthetic graphite materials with hierarchical pores from lignite by one-step impregnation and their characterization as dye absorbents, RSC Adv. 9 (2019) 12737–12746.
[63] Z.Q. Li, C.J. Lu, Z.P. Xia, Y. Zhou, Z. Luo, X-ray diffraction patterns of graphite and turbostratic carbon, Carbon 45 (2007) 1686–1695.
[64] A.C. Ferrari, J.C. Meyer, V. Scardaci, C. Casiraghi, M. Lazzeri, F. Mauri, S. Piscanec, D. Jiang, K.S. Novoselov, S. Roth, A.K. Geim, Raman spectrum of graphene and graphene layers, Phys. Rev. Lett. 97 (2006) 187401.
[65] J. Hong, M.K. Park, E.J. Lee, D. Lee, D.S. Hwang, S. Ryu, Origin of new broad Raman D and G peaks in annealed graphene, Sci. Rep. 3 (2013) 2700.
[66] B. Lesiak, L. Kövér, J. Tóth, J. Zemek, P. Jiricek, A. Kromka, N. Rangam, C sp2/sp3 hybridisations in carbon nanomaterials – XPS and (X)AES study, Appl. Surf. Sci. 452 (2018) 223–231.
[67] A. Fujimoto, Y. Yamada, M. Koinuma, S. Sato, Origins of sp3C peaks in C1s X-ray photoelectron spectra of carbon materials, Anal. Chem. 88 (2016) 6110–6114.